Calculation of the Temperature Field in Injection Molding

The numerical simulation of nonisothermal effects during the filling stage of injection molding is investigated here. Generalized Newtonian fluid flows are simulated within thin cavities of arbitrary shape. The numerical scheme is based on a hybrid spatial discretization: classical low-order Lagrangian interpolants are used in the midsurface directions, while full polynomials constitute the approximation in the gapwise direction. Discrete equations are obtained by use of the Galerkin finite element method combined with a collocation procedure. Special attention is devoted to the influence of the fountain flow (occurring at the front) on the temperature field. A correct writing of the front thermal boundary condition is derived in agreement with the Hele-Shaw simplified form of the equations. Some illustrative results are presented.

F. Dupret and L. Vanderschuren
Unité de Mécanique Appliquée
Université Catholique de Louvain
B-1348 Louvain-la-Neuve, Belgium

Introduction

Thermal exchanges play an important role in injection molding, in view of their influence on polymer freezing and shrinkage during the cooling stage of the process. As the thermal behavior of the polymer during cooling is conditioned by the temperature field which prevails after completion of the filling and packing stages, it is essential to accurately calculate the thermal evolution during the filling of the cavity.

Among previous investigations on the same topic, the works of Williams and Lord (1975) and Lord and Williams (1975) are of outstanding importance. Using a method of finite differences, they obtain nonisothermal solutions for the filling of one-dimensional cavities. They also simulate the flow in the sprue, runner and gate system of the mold. In addition, the contributions of Hieber and Shen (1980), Shen (1986), and Hieber (1987) must be cited. The latter authors introduce a finite element discretization of the covered part of the midsurface of the mold to facilitate the treatment of cavities of general planar geometry. Moreover, they use finite differences for the temperature discretization in the gapwise direction.

The difficulty of the problem is that one is facing a three-dimensional, transient and variable domain system of partial differential equations. On the one hand, this is a consequence of the complex motion of the melt front during filling, Figure 1, and on the other, of the inherent nature of the energy equation (which is a balance among heat diffusion, heat advection, and viscous heating in the polymer). An additional feature is that a decoupling of momentum and energy equations is not allowed in the model. As a matter of fact, thermal exchanges have an influence on the velocity profile in the gap and may considerably affect the geometry of the pathlines and the filling history, since the polymer viscosity is temperature-dependent and partial solidification generally occurs near the cold walls of the cavity.

Consequently, it seems to be a very expensive task to obtain numerical solutions, particularly when keeping in mind the geometrical complexity of common industrial molds. However, following Schlichting (1968) and all the previously mentioned authors, important simplifications may be performed on the model by introducing the Hele-Shaw approximation, which is closely related to lubrication theory and applies in the case of thin molds. The resulting system of equations is two-dimensional for the pressure field, and remains three-dimensional for the temperature field.

Difficulty then appears in correctly writing the associated front thermal boundary conditions. The problem may be summarized as follows: the velocity field obtained by applying the Hele-Shaw method is approximately parallel to the midsurface, whereas, in the front region of the flow, the fountain effect induces an important heat advection in the gap direction. A suitable handling of the latter effect is, therefore, required in the model to protect the system from undue heat losses at the front.

To this end, a complex modeling of fountain flow was developed in Castro and Macosko (1982). The solution of Lord and Williams (1975), Hieber and Shen (1980), and Shen (1986) consists in simplifying the model by imposing a uniform temperature on the front, the latter being either the bulk temperature as measured immediately upstream of the melt front or some core temperature. We consider that this method is not com-

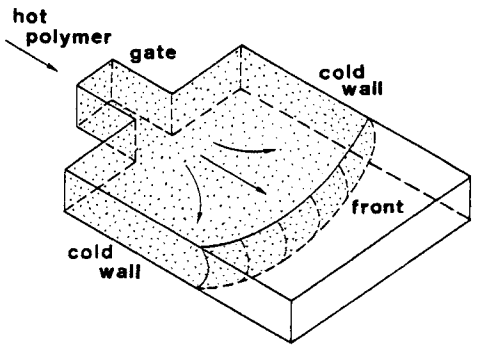

Figure 1. Schematic view of the problem.

pletely satisfactory from a mathematical view point, since it leads to an ill-posed problem (in the sense of theory of partial differential equations). We propose a new solution, which is mathematically correct and yields a well-posed simplified thermal problem.

The numerical scheme presented here combines finite element interpolation in the midsurface directions, as in Hieber and Shen (1980), and full polynomial approximation in the gapwise direction, which accurately represents the temperature gradient near the walls with a reduced number of unknowns. At any time step, the mesh covering the filled part of the midsurface is generated by means of a separately developed algorithm (Couniot and Crochet, 1986). Time integration of the temperature field is performed using a specially devoted mixed explicit-implicit scheme to ensure stability and precision. A peculiar treatment of the front thermal boundary condition arising from fountain flow is also necessary.

Some results are displayed in the last section of the paper and show up the major influence of fountain flow on the resulting temperature field. The final average isotherms are in agreement with the result expected from physical reasoning. A first attempt is also made to simulate partial solidification of the fluid during filling.

Approximate solidified-layer profiles were calculated by Janeschitz-Kriegl (1977, 1979), Dietz and White (1978), and Van Wijngaarden et al. (1982). A theoretical analysis of freezing during filling was presented by Richardson (1983). Entry and trailing thermal boundary layers in the melt were analyzed by Tayler and Nicholas (1982). Experimental results of Coyle et al. (1987) illustrate the behavior of the fountain flow.

Governing Equations

Field equations

We consider the creeping flow of a generalized Newtonian fluid, with a viscosity dependence on the absolute temperature T and the shear rate $\dot{\gamma}$. We assume that elastic effects are negligible. The viscosity is given by a power law of the form:

$$\mu(\dot{\gamma}, T) = m(T)\,\dot{\gamma}^{n-1}, \tag{1}$$

where n is the power index and $m(T)$ is a material function. For many materials, a fairly good approximation for $m(T)$ is the exponential law:

$$m(T) = m_o\, e^{-aT}, \tag{2}$$

as long as the temperature is far from the melting temperature T_m. We will also assume here that the polymer thermal conductivity k, specific heat c, and specific mass ρ do not depend on temperature.

We must solve the mass, momentum and energy conservation laws. The mathematical system is closed by suitable front, inlet and wall boundary conditions, which are supposed to be symmetric with respect to the midsurface. The problem is simplified by taking into account the small thickness of the gap compared to the characteristic dimensions and radii of curvature of the mold. In the case of a variable mold thickness $2h$, we also assume that the derivatives of $2h$ in the midsurface directions are small compared to one.

The simplified form of the equations must be achieved by means of dimensional analysis, following the method of Hele-Shaw (Schlichting, 1968). The latter was applied to the injection molding problem in the case of a flat midsurface by Lord and Williams (1975) and Hieber and Shen (1980). We here extend it to the case of nonplanar midsurfaces.

Let us now examine the equations in detail. At any point P^* of the midsurface S_m, an orthonormal frame (ξ, η, ζ) is defined such that $P^*\zeta$ is normal to S_m; this implies that $P^*\xi$ and $P^*\eta$ are tangent to the latter surface, Figure 2. At any point P of $P^*\zeta$, the velocity v is split into two components, one (v_m) being parallel to the midsurface, while the other $(v_\zeta g_\zeta)$ is oriented along $P^*\zeta$:

$$\begin{cases} v = v_m + v_\zeta g_\zeta, \\ v_m = v_\xi g_\xi + v_\eta g_\eta. \end{cases} \tag{3}$$

We assume no-slip condition along the walls and thus:

$$\begin{cases} v_m(\zeta = \pm h) = \mathbf{0}, \\ v_\zeta(\zeta = \pm h) = 0. \end{cases} \tag{4}$$

Letting the symbol ∇_m stand for the midsurface constrained gradient operator, the simplified forms of the mass and momentum equations are:

$$\nabla_m \cdot v_m + \frac{\partial v_\zeta}{\partial \zeta} = 0, \tag{5}$$

$$\frac{\partial}{\partial \zeta}\left(\mu \frac{\partial v_m}{\partial \zeta}\right) = \nabla_m p, \tag{6}$$

$$\frac{\partial p}{\partial \zeta} = 0. \tag{7}$$

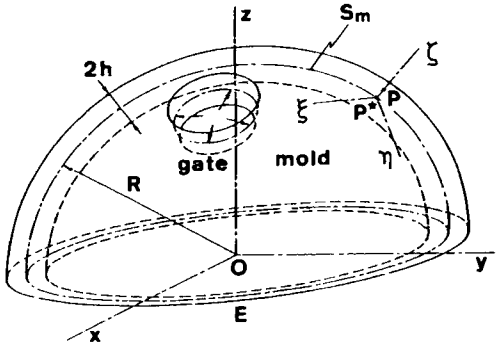

Figure 2. Semispherical geometry.

The shear rate $\dot{\gamma}$ and the viscosity μ are aproximated by:

$$\dot{\gamma} = \left\| \frac{\partial v_m}{\partial \zeta} \right\|, \tag{8}$$

$$\mu = m(T) \left\| \frac{\partial v_m}{\partial \zeta} \right\|^{n-1}. \tag{9}$$

Equation 7 tells us that pressure variation in the thickness of the mold is negligible (which in fact is the lubrication approximation).

It is easy to integrate Eq. 6 with respect to ζ by means of wall conditions (Eq. 4) and the viscosity law (Eq. 1). Assuming symmetry with respect to the midsurface, this yields:

$$v_m(\zeta) = -\nabla_m p \, \|\nabla_m p\|^{1/n-1} \int_\zeta^h \left(\frac{\tilde{\zeta}}{m(T)} \right)^{1/n} d\tilde{\zeta}. \tag{10}$$

Let $\bar{v}$ stand for the average velocity, parallel to the midsurface S_m:

$$h\bar{v} = \int_0^h v_m \, d\zeta. \tag{11}$$

Introducing Eq. 10 in Eq. 11 yields:

$$h\bar{v} = -S \, \nabla_m p, \tag{12}$$

where the symbol S is defined by

$$S = \|\nabla_m p\|^{1/n-1} \int_0^h \left(\frac{\zeta}{m(T)} \right)^{1/n} \zeta \, d\zeta. \tag{13}$$

By averaging the continuity equation (Eq. 5) over the thickness of the mold, one obtains

$$\nabla_m \cdot (-S \, \nabla_m p) = 0. \tag{14}$$

For a given temperature distribution, the expression $m(T)$ is known explicitly, and Eq. 14 is a second-order partial differential equation on the pressure field.

Associated boundary conditions are of two kinds: the pressure p or the normal component $(\bar{v} \cdot n)$ of the average velocity are prescribed on any inlet gate, while the pressure is imposed on the flow front.

The energy equation takes the following simplified form:

$$\frac{DT}{Dt} = \frac{k}{\rho c} \frac{\partial^2 T}{\partial \zeta^2} + \frac{\mu}{\rho c} \left\| \frac{\partial v_m}{\partial \zeta} \right\|^2. \tag{15}$$

The first and second terms of the righthand side of Eq. 15 are respectively associated with heat diffusion (which prevails in the gapwise direction) and viscous heating. The lefthand side of Eq. 15 is the material derivative of the temperature, which may be decomposed as follows:

$$\frac{DT}{Dt} = \frac{\partial T}{\partial t} + v \cdot \nabla T$$

$$= \frac{\partial T}{\partial t} + v_m \cdot \nabla_m T + v_\zeta \frac{\partial T}{\partial \zeta}. \tag{16}$$

For a given pressure field, the average velocities $\bar{v}$ may be calculated from Eqs. 12 and 13. The v_m component of the velocity field may thereafter be obtained from Eq. 10. The v_ζ component should also be obtained by integrating Eq. 5 with the wall condition (Eq. 4). However, when the mold thickness is constant, the thermal convection term in the gapwise direction $(v_\zeta \partial T/\partial \zeta)$ is at the present time neglected in our computations. When the mold thickness is variable, the velocity component v_ζ is approximated by the expression

$$v_\zeta = (v_m \cdot \nabla_m h) \frac{\zeta}{h}, \tag{17}$$

which means that we consider only a locally convergent, divergent or parallel approximate velocity field, Figure 3. Equation 17 is the exact solution of Eqs. 5 and 4 with Eqs. 3, 10, 13 and 14 in the Newtonian isothermal case. For a given velocity field, Eq. 15 is a second order (for ζ derivatives) and first order (for all other derivatives) evolution equation on the temperature field. Boundary conditions consist in imposing the initial temperatures and the inlet temperature profile. Boundary conditions on the front and the walls play a major role in the model and will be investigated separately in the next subsection.

Let us briefly turn back our attention to the asymptotical forms (Eqs. 5, 6, 7 and 15) of the field equations. The latter can be obtained from the full mass, momentum and energy equations by letting tend towards zero the dimensionless number ϵ defined by:

$$\epsilon = \frac{\delta}{L}, \tag{18}$$

where δ is the order of magnitude of the mold thickness and L is any characteristic dimension or radius of curvature of the midsurface. The complete demonstration uses tensor analysis methods and notations and is developed in Dupret and Vanderschuren (1988).

Front and wall boundary conditions: fountain flow modeling

At any time of the filling, we need to distinguish between two regions in the filled area: upstream of the front, the flow is essentially parallel to the walls and Hele-Shaw's approximation applies, whereas velocities are strongly deflected towards the walls in the vicinity of the front. Concerning an accurate simulation of the so-called fountain effect, the interested reader will find more detail and references in, for example, Behrens et al. (1987). Moreover, a comparison between experimental and numerical results can be found in Coyle et al. (1987). However, our aim here is different, because our purpose is only to investigate the influence of the fountain effect on the main flow in the form of suitable boundary conditions.

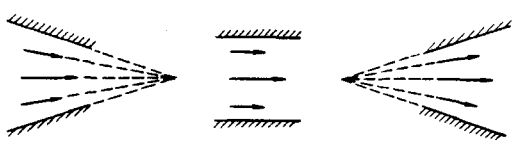

Figure 3. Approximation of the v_ζ component in the temperature equation.

Let us first analyze in Figure 4 the relative motion of the fluid with respect to the front. The flow is steady and the average fluid velocity vanishes, while the walls move in the negative ξ direction. This well-known result shows that the region of parallel flow (located at the lefthand side of the segment AB) is divided in a central subregion and a wall subregion, where the relative fluid velocity is respectively oriented in the positive or the negative ξ direction. The front region is, therefore, fed (through the segment AC) with fluid that flows out of the central subregion of the upstream flow, whereas the wall subregion is fed with fluid that flows out of the front region (through the segment CB).

Turning back our attention to the absolute motion of the fluid (*with respect to* fixed walls), we conclude that the front region is continuously fed with fluid issued from central layers. Material points leaving this subregion are entering the front region at a velocity which is higher than the front velocity. After a rolling motion in the front, the latter points leave this region at a velocity which is lower than the front velocity and enter again the region of parallel flow; more precisely, they enter the wall subregion of the latter.

A proper fountain flow model must be built in agreement with the Hele-Shaw simplified form of the equations. To this end, two basic assumptions are made. On the one hand, the front region is supposed to be of the same order of magnitude as the thickness of the gap. As only asymptotical equations are used, this implies that the front region is infinitely thin and made of straight segments perpendicular to the midsurface. Equivalently, at any fixed time, the front is a set of straight segments of the form:

$$\begin{cases} (\xi, \eta) = \text{constants}, \\ -h(\xi, \eta) \le \zeta \le h(\xi, \eta). \end{cases} \tag{19}$$

On the other hand, we suppose that velocities in the front region are of the same order of magnitude as the average velocity over the gap. The residence time of material points in the front region is, therefore, small compared with the characteristic time scale of the filling [their ratio is indeed (from Eq. 18) of the order $O(\epsilon)$]. We are, therefore, allowed to neglect asymptotically heat diffusion and viscous heating in the front region.

As a main consequence of the latter assumptions, an additional thermal boundary condition must be imposed on the front when using the asymptotical forms of the equations. Consider any material point entering the front at the level $\zeta_{(1)}$ and leaving the front at the level $\zeta_{(2)}$, Figure 5. From mass conservation, couples of levels $\zeta_{(1)}$ and $\zeta_{(2)}$ are related by the condition:

$$\int_0^{\zeta_{(1)}} (v - \bar{v}) \cdot \boldsymbol{n}\, d\zeta = \int_{\zeta_{(2)}}^{h} (\bar{v} - v) \cdot \boldsymbol{n}\, d\zeta, \tag{20}$$

where $\boldsymbol{n}$ is the outgoing front normal. Neglecting heat diffusion and viscous heating in the front layer, we, therefore, impose the condition:

$$T(\xi, \eta, \zeta_{(2)}) = T(\xi, \eta, \zeta_{(1)}), \tag{21}$$

which ensures the well-posedness of the asymptotical thermal problem. [For the definition of the latter concept, see, for example, Hadamard (1964).] As a matter of fact, the temperature of material points entering the front layer cannot be imposed, while it must be imposed for material points leaving it, since, from Eq. 15, heat diffusion in the midsurface direction is neglected in the region of parallel flow.

Due to the dependence of viscosity vs. temperature (Eq. 9), the velocity profile is unknown *a priori* in nonisothermal problems, which is why relation 20 is difficult to handle numerically. However, we shall neglect the latter effect, assuming that temperature variations in the gap are small on the front. Recall indeed the front feeding with central and rapidly moving fluid layers, whence front and gate temperatures are generally close together. Using Eqs. 10 and 13 with a nontemperature-dependent viscosity law, Eq. 20 simplifies after some calculations in the algebraic condition:

$$\zeta_{(2)}\left(1 - \left(\frac{\zeta_{(2)}}{h}\right)^{1/n+1}\right) = \zeta_{(1)}\left(1 - \left(\frac{\zeta_{(1)}}{h}\right)^{1/n+1}\right), \tag{22}$$

which is used in all practical computations.

The idea of approximating the fountain flow by flipping over the material points (Eqs. 20 and 22, and Figure 5) has also been developed by Manas-Zloczower et al. (1987) for the calculation of space-time distributions of particles in reaction injection molding. However, the present work has been done independently (Vanderschuren and Dupret, 1987) with special attention to a proper modeling of thermal exchanges in the vicinity of the front (Eq. 21). A complete demonstration of the asymptotical behavior of the system (Eqs. 19 to 21) has been developed by Dupret and Vanderschuren (1988).

Suitable transient boundary conditions must be imposed on the walls. As a matter of fact, the front central layer ($\zeta_{(1)} = 0$) is carried exactly on the wall ($\zeta_{(2)} = h$) by the fountain flow. The front thermal condition (Eq. 21) will, therefore, induce on the front-wall junction either a temperature discontinuity (when imposing the wall temperature) or a temperature gradient dis-

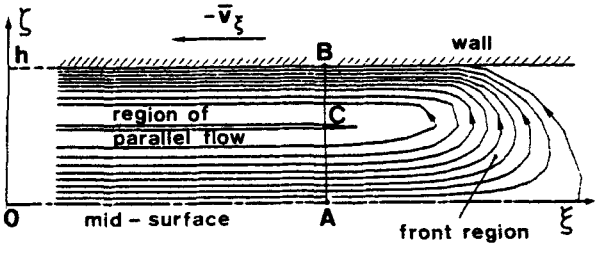

Figure 4. Fountain effect: computed streamlines in the *relative motion of the fluid with respect to the* front (isothermal Stokes flow).

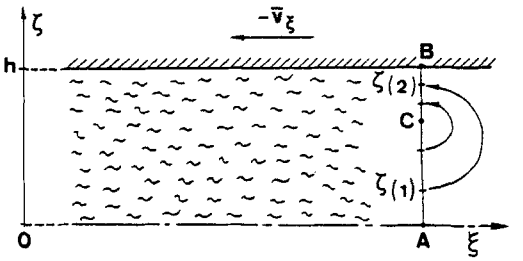

Figure 5. Fountain flow modeling.

continuity (when imposing the wall outgoing heat flux). In order to get rid of any singularity in the temperature field, transient thermal exchanges occurring in the wall are taken into account in the model.

We suppose that, from some distance e inside the wall, Figure 6, temperatures are almost constant (and equal to T_e), and we approximate the wall temperature field up to this distance by a cubic polynomial:

$$T(\zeta) = a + b\zeta + c\zeta^2 + d\zeta^3, \quad h \le \zeta \le h + e, \tag{23}$$

where coefficients a, b, c and d depend on the ξ, η and t independent variables. Assuming that the distance e is of the same order of magnitude as the thickness of the gap ($2h$), we neglect ξ and η derivatives in the energy equation inside the wall. Hence, the latter takes the form

$$\rho_s c_s \frac{\partial T}{\partial t} = k_s \frac{\partial^2 T}{\partial \zeta^2}, \tag{24}$$

where ρ_s, c_s and k_s are the wall specific mass, specific heat, and thermal conductivity, respectively. Coefficients a, b, c and d are then expressed in terms of the temperatures and heat fluxes at $\zeta = h$ and $\zeta = h + e$, i.e.:

$$\begin{cases} T_w = T(h), \quad T_e = T(h+e), \\ q_w = -k_s \dfrac{\partial T}{\partial \zeta}(h^+) = -k \dfrac{\partial T}{\partial \zeta}(h^-), \quad q_e = -k_s \dfrac{\partial T}{\partial \zeta}(h+e^-). \end{cases} \tag{25}$$

Collocation of Eq. 24 at $\zeta = h$ and $\zeta = h + e$ provides two relations between T_w, T_e, $\partial T_w/\partial t$, $\partial T_e/\partial t$, q_w and q_e. The required boundary condition is then obtained by elimination of q_e between the latter equations:

$$\frac{e\rho_s c_s}{6}\left(\frac{\partial T_e}{\partial t} + 2\frac{\partial T_w}{\partial t}\right) - \frac{k_s}{e}(T_e - T_w) - q_w = 0. \tag{26}$$

Numerical Method

Spatial discretization

The numerical scheme is based on a hybrid spatial discretization. Classical low-order Lagrangian interpolants are used in the midsurface directions, while full polynomials are used in the gapwise direction. Discrete equations are obtained by combining the Galerkin finite element method with a Chebyshev collocation procedure. The latter choice is justified by the exponential rate of convergence of this method (Gottlieb and Orszag, 1977).

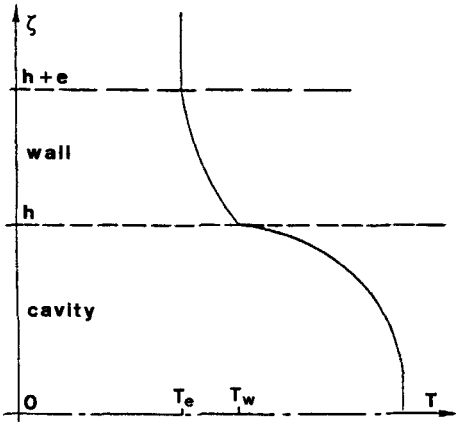

Figure 6. Schematic temperature profile in the cavity and the wall.

The filled part S_m^* of the midsurface is covered by a finite element mesh. Elements may be either six-node triangles or nine-node quadrilaterals. Therefore, nonplanar elements are possible. Let $\hat{\xi}$ and $\hat{\eta}$ be the local coordinates on the parent element, and (x, y, z) be a common global orthonormal system of Cartesian coordinates. For each element, the local to global transformation has the form:

$$x = x(\hat{\xi}, \hat{\eta}), \quad y = y(\hat{\xi}, \hat{\eta}), \quad z = z(\hat{\xi}, \hat{\eta}). \tag{27}$$

At the present time, the front motion and remeshing algorithm is limited to planar molds, with rectilinear-sided elements (Couniot and Crochet, 1986). Extensions are under investigation. However, pressure and temperature integration may now be performed on any surface, following the method presented below.

The pressure field is approximated using six-node quadratic or nine-node biquadratic shape functions $\psi_i(\hat{\xi}, \hat{\eta})$ defined on the parent element:

$$p = \sum_i p_i \psi_i(\hat{\xi}, \hat{\eta}), \tag{28}$$

where the p_i's are the pressure nodal values.

The mass equation (Eq. 14) is discretized by means of the Galerkin method, which yields

$$\int_{S_m^*} S(\nabla_m p \cdot \nabla_m \psi_i)\, d\sigma = \int_{\partial S_m^*} S \frac{\partial p}{\partial n} \psi_i \, ds, \tag{29}$$

where the symbol S has been defined in Eq. 13 and $\boldsymbol{n}$ denotes the midsurface constrained outer normal on ∂S_m^*. Essential and natural boundary conditions on the pressure and velocity fields must be properly introduced in Eq. 29 at this stage, either by annulling the test functions ψ_i at any node of imposed pressure or by substituting in Eq. 29 the prescribed value of $(h\bar{v} \cdot \boldsymbol{n})$ for $(-S\partial p/\partial n)$.

In the case of a nonplanar midsurface, one needs to calculate $\nabla_m p$ and $\nabla_m \psi_i$ on each element of S_m^*. Let the three Cartesian components of $\nabla_m p$ in the (x, y, z) reference system be $\partial p/\partial x$, $\partial p/\partial y$ and $\partial p/\partial z$. It is easy to prove that:

$$\left[\frac{\partial p}{\partial x}\frac{\partial p}{\partial y}\frac{\partial p}{\partial z}\right]^T = A^T(AA^T)^{-1}\left[\frac{\partial p}{\partial \hat{\xi}}\frac{\partial p}{\partial \hat{\eta}}\right]^T, \tag{30}$$

where

$$A = \begin{bmatrix} \dfrac{\partial x}{\partial \hat{\xi}} & \dfrac{\partial y}{\partial \hat{\xi}} & \dfrac{\partial z}{\partial \hat{\xi}} \\ \dfrac{\partial x}{\partial \hat{\eta}} & \dfrac{\partial y}{\partial \hat{\eta}} & \dfrac{\partial z}{\partial \hat{\eta}} \end{bmatrix} \tag{31}$$

From Eqs. 27, 30 and 31, it follows that the three components of $\nabla_m p$ are known in terms of the pressure derivatives with respect to the local coordinates $\hat{\xi}$ and $\hat{\eta}$.

For a given temperature field, Eq. 29 provides an algebraic system in the pressure nodal values. This system is linear if the fluid is Newtonian. Otherwise, Newton's method may be used to obtain the solution.

Mixed approximation is used for the temperature field: three-node linear or four-node bilinear shape functions $\phi_i(\hat{\xi}, \hat{\eta})$ are employed in the midsurface directions, combined with even polynomials of some fixed degree $2m$ in the gapwise direction. Let

$$\hat{\zeta} = \frac{\zeta}{h}, \tag{32}$$

denote a normalized coordinate which vanishes on the midsurface and equals ± 1 on the walls. The temperature approximation is written as:

$$T = \sum_i T_i(\hat{\zeta}, t)\, \phi_i(\hat{\xi}, \hat{\eta}). \tag{33}$$

For each node i of the midsurface, $T_i(\hat{\zeta}, t)$ represents the polynomial temperature profile in the gap at time t. Let $\hat{\zeta}_\alpha (1 \le \alpha \le m)$ be a set of m collocation points and $Q_\alpha(\hat{\zeta})$ be the m associated Lagrange interpolation polynomials, which vanish at $\hat{\zeta} = \pm 1$. Observe that

$$Q_\alpha(\hat{\zeta}_\beta) = \delta_{\alpha\beta}, \tag{34}$$

where $\delta_{\alpha\beta}$ is the Kronecker symbol. Expression $T_i(\hat{\zeta}, t)$ is developed as

$$T_i(\hat{\zeta}, t) = T_{iw}(t) + \sum_\alpha (T_{i\alpha}(t) - T_{iw}(t))\, Q_\alpha(\hat{\zeta}), \tag{35}$$

where $T_{iw}(t)$ and $T_{i\alpha}(t)$ are the unknown values of the temperature at node i and time t, on the wall or at collocation point α, respectively.

Spatial discretization of the temperature equation (Eq. 15) is performed in two steps. In the first step, the Galerkin method is applied in the midsurface directions and provides equations over the set of $T_i(\hat{\zeta}, t)$ functions. In the second step, collocation is applied on the resulting equation at the m points $\hat{\zeta}_\alpha$. The selected collocation points are the zeroes of the $2m$-degree Chebyshev polynomial

$$T_{2m}(\hat{\zeta}) = \cos(2m \cos^{-1} \hat{\zeta}), \tag{36}$$

which gives

$$\hat{\zeta}_\alpha = \cos\left[(2\alpha - 1)\frac{\pi}{4m}\right]. \tag{37}$$

The latter choice is justified by the excellent convergence properties of the Chebyshev polynomials. Moreover, collocation points are in this manner piled up in the vicinity of the walls, where velocity and temperature gradients are important. The resulting semidiscrete system of equations is

$$\sum_j \left[\dot{T}_{j\alpha} - \sum_\beta \frac{k}{h_j^2 \rho c} Q''_\beta(\hat{\zeta}_\alpha)\,(T_{j\beta} - T_{jw})\right] \int_{S_m^*} \phi_i\, \phi_j\, d\sigma = \int_{S_m^*} \left[-\boldsymbol{v} \cdot \nabla T + \frac{\mu}{\rho c}\dot{\gamma}^2\right]_{\hat{\xi}-\hat{\xi}_\alpha} \phi_i\, d\sigma, \tag{38}$$

where $\boldsymbol{v} \cdot \nabla T$ is computed using approximation (Eq. 17).

The latter system is completed by the wall boundary condition (Eq. 26), which for constant T_e is written as:

$$\sum_j \left[\dot{T}_{jw} + \frac{3k_s}{e^2 \rho_s c_s} T_{jw} + \frac{3k}{h_j e \rho_s c_s} \sum_\alpha Q'_\alpha(1)\,(T_{j\alpha} - T_{jw})\right] \int_{S_m^*} \phi_i\, \phi_j\, d\sigma = \int_{S_m^*} \frac{3k_s}{e^2 \rho_s c_s} T_e\, \phi_i\, d\sigma. \tag{39}$$

The full system is, therefore, of the matrix form

$$M([\dot{T}] - K[T]) = q([T], [p]), \tag{40}$$

where $[T]$ and $[p]$ are the vectors of all unknowns $T_{i\alpha}$, T_{iw}, and p_i. We may observe that, for suitable permutations of rows and columns, the matrix K (associated with thermal diffusion) is block-diagonal, each block having order $(m + 1)$, and that the mass matrix M is positive definite and block-diagonal, with $(m + 1)$ blocks equal to $\int_{S_m^*} \phi_i \phi_j\, d\sigma$. All the terms arising from heat transport and viscous heating are included in the vector $q([T], [p])$. The velocity field must be calculated by the pressure Eq. 29 which is of the matrix form

$$G([p], [T])[p] = r, \tag{41}$$

with a stiffness matrix G depending on the pressure and temperature fields via the symbol S.

Time integration

After calculation of the pressure field on the proper temporary mesh, Eq. 40 is integrated over one time interval using the same mesh. In order to ensure stability and precision, this integration is performed by means of a third order mixed explicit-implicit scheme. It is worth noting that only single-step methods are available, since a new mesh is provided at each time step by the remeshing algorithm. [For any question related to numerical time integration, see, for example, Jain (1979).] After time integration, the temperature field is extrapolated on the new mesh according to the front thermal condition (Eq. 21), following the method developed in the next subsection.

In order to achieve stability, the proposed integration scheme is implicit for the treatment of diffusive terms (Hieber and Shen, 1980). Related eigenvalues of the associated linearized problem are indeed real, negative and of the order of magnitude $O(k/\rho c h^2)$, whence a fully explicit scheme would lead to strong instabilities in the case of a small gap thickness $2h$. Considering Eq. 40, we observe that linear systems involving the matrix K (associated with heat diffusion) are easily solved, due to the block structure of the latter matrix. An implicit treatment of the corresponding terms is, therefore, possible.

The remaining terms in Eq. 40 arise from heat advection and viscous heating. An explicit treatment is required for preserving

computing time. We have selected the fourth-order Runge-Kutta method to achieve stability and precision. As a matter of fact, this method is conditionally stable on the imaginary axis (Lapidus and Seinfeld, 1971). Moreover, pure advection problems have antisymmetric matrices with purely imaginary eigenvalues when the Galerkin method is not combined with any upwinding technique. Note that the third-order Runge-Kutta method is also a possible choice.

A mixed explicit-implicit scheme is obtained in the following way. We first put the system (Eq. 40) in the more concise form

$$\dot{\tilde{y}} = K\tilde{y} + f(\tilde{y}), \tag{42}$$

where

$$\begin{cases} \tilde{y} = [T], \\ f(\tilde{y}) = M^{-1}q([T], [p]). \end{cases} \tag{43}$$

We observe that calculation of $f(\tilde{y})$ is cheap, since only one LL^T Cholesky factorization of one of the blocks $\int_{S_m^*} \phi_i\phi_j \, d\sigma$ of the matrix M is required. The proposed scheme is of the general form:

$$\begin{cases} k_1 = K\tilde{y}_n + f(\tilde{y}_n), \\ k_2 = K\left[\tilde{y}_n + \dfrac{\Delta t}{2}(\theta_{22}k_2 + (1-\theta_{22})k_1)\right] + f\left(\tilde{y}_n + \dfrac{\Delta t}{2}k_1\right), \\ k_3 = K\left[\tilde{y}_n + \dfrac{\Delta t}{2}(\theta_{33}k_3 + \theta_{32}k_2 \right. \\ \qquad \left. + (1-\theta_{33}-\theta_{32})k_1)\right] + f\left(\tilde{y}_n + \dfrac{\Delta t}{2}k_2\right), \\ k_4 = K\{\tilde{y}_n + \Delta t[\theta_{44}k_4 + \theta_{43}k_3 + \theta_{42}k_2 \\ \qquad + (1-\theta_{44}-\theta_{43}-\theta_{42})k_1]\} + f(\tilde{y}_n + \Delta t k_3), \\ \tilde{y}_{n+1} = \tilde{y}_n + \dfrac{\Delta t}{6}(k_1 + 2k_2 + 2k_3 + k_4), \end{cases} \tag{44}$$

where $\tilde{y}_n$ and $\tilde{y}_{n+1}$ are the values of $\tilde{y}$ at times t_n and t_{n+1}, and Δt is the time interval $(t_{n+1} - t_n)$. Coefficients θ_{pq} are calculated in such a way that the method has an improved stability and is of the third order.

The stability analysis is performed separately for the terms arising from $f(\tilde{y})$ and $K\tilde{y}$ in Eq. 44. If the matrix K vanishes, the scheme reduces to the classical fourth order Runge-Kutta method, whence, for any linear $f(\tilde{y})$ of the form:

$$f(\tilde{y}) = B\tilde{y}, \tag{45}$$

the scheme is stable if the eigenvalues λ_i of B satisfy the inequalities

$$\begin{cases} 0 > \lambda_i > -2.785, & \text{if } \lambda_i \text{ is real,} \\ |\lambda_i \Delta t| < 2.828, & \text{if } \lambda_i \text{ is imaginary.} \end{cases} \tag{46}$$

The general case of complex eigenvalues was analyzed by Lapidus and Seinfeld (1971).

If $f(\tilde{y})$ vanishes, linear stability is observed if, for any eigenvalue λ_i of the matrix K, the so-called amplification factor $E(-\lambda_i\Delta t)$ has a modulus inferior to one. The latter is obtained by reducing $K\tilde{y}$ to $\lambda\tilde{y}$ in the scheme, with the definition

$$E(-\lambda\Delta t) = \frac{\tilde{y}_{n+1}}{\tilde{y}_n}. \tag{47}$$

Here, $E(-\lambda\Delta t)$ is obviously a rational function of $\tilde{z} = -\lambda\Delta t$. We have restricted our analysis to amplification factors of the form:

$$E(\tilde{z}) = \frac{a'}{1+b\tilde{z}} + \frac{a''}{(1+b\tilde{z})^2} + \frac{a'''}{(1+b\tilde{z})^3}, \tag{48}$$

which might be associated with strongly A-stable schemes.

The method is of the third order only if

$$E(\tilde{z}) = e^{-\tilde{z}} + o(\tilde{z}^3), \tag{49}$$

whence, after some calculations,

$$\begin{cases} a' = \dfrac{1}{2b^3} - \dfrac{4}{b^2} + \dfrac{6}{b}, \\ a'' = -\dfrac{1}{2b^3} + \dfrac{7}{2b^2} - \dfrac{4}{b}, \\ a''' = \dfrac{1}{6b^3} - \dfrac{1}{b^2} + \dfrac{1}{b}, \end{cases} \tag{50}$$

and

$$b^3 - 3b^2 + \frac{3}{2}b - \frac{1}{6} = 0. \tag{51}$$

The roots of the latter equation are given by:

$$\begin{cases} b_1 = 1 + \sqrt{2}\cos\omega, \\ b_2 = 1 + \sqrt{2}\cos(\omega + 2\pi/3), \\ b_3 = 1 + \sqrt{2}\cos(\omega - 2\pi/3), \end{cases} \tag{52}$$

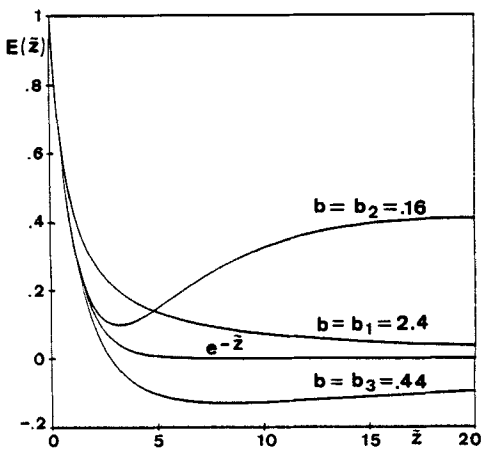

Figure 7. Amplification factors for the proposed third order scheme.

with

$$\omega = \frac{1}{3}\cos^{-1}\frac{2\sqrt{2}}{3}. \tag{53}$$

The corresponding amplification factors $E(\tilde{z})$ are plotted on Figure 7 for positive values of $\tilde{z}$. After some trials, the root b_3 was chosen, as providing the best numerical results.

Turning back our attention to the global scheme (Eq. 44), the amplification factor will be the selected function if

$$\begin{cases} \theta_{22} = \theta_{33} = 2\theta_{44} = 2b, \\ \theta_{43} + \theta_{42} + \theta_{32} = 2 - 6b, \\ \theta_{43}\theta_{32} = 4b(1 - 6b + 6b^2). \end{cases} \tag{54}$$

A peculiar solution of the last two equations is:

$$\begin{cases} \theta_{43} = 1 - 3b - (1 - 10b + 33b^2 - 24b^3)^{1/2}, \\ \theta_{32} = 1 - 3b + (1 - 10b + 33b^2 - 24b^3)^{1/2}, \\ \theta_{42} = 0. \end{cases} \tag{55}$$

Time step control may be achieved by means of the following method: a second solution is computed using reduced time substeps; the error is evaluated by comparing both results and taking into account the order of the scheme.

Simulation of the fountain flow

Time integration of the energy equation is performed on the initial mesh of any time interval $[t_n, t_{n+1}]$ and must, therefore, be followed by a suitable extrapolation of the temperature field on the new mesh (provided after front motion by the remeshing algorithm). The front thermal condition (Eq. 21) arising from the fountain effect is here taken into account and will have an influence only in the region located between two successive fronts.

Let R_n be the mesh at time t_n, R_{n+1} be the mesh at time t_{n+1}, and S_m^n and S_m^{n+1} be the corresponding flow domains on the midsurface, Figure 8. Let $\hat{T}^{n+1}(r, \hat{\zeta})$, with

$$r \in S_m^n, \quad 0 \le \hat{\zeta} \le 1, \tag{56}$$

be the temperature field as obtained after time integration on the mesh R_n. We wish now to evaluate $T^{n+1}(r, \hat{\zeta})$, with

$$r \in S_m^{n+1}, \quad 0 \le \hat{\zeta} \le 1, \tag{57}$$

on the new mesh R_{n+1}.

To this end, a least square approximation is performed. The expression

$$F(T^{n+1}, \hat{T}^{n+1}) = \int_{S_m^{n+1}} [T^{n+1}(r, \hat{\zeta}) - \hat{T}^{n+1}(r, \hat{\zeta})]^2 \, d\sigma, \tag{58}$$

is minimized on the wall ($\hat{\zeta} = 1$) and for any collocation point ($\hat{\zeta} = \hat{\zeta}_\alpha$). Equivalently, we must solve the linear systems

$$\sum_j T_j^{n+1}(\hat{\zeta}) \int_{S_m^{n+1}} \phi_i \phi_j \, d\sigma = \int_{S_m^{n+1}} \phi_i \hat{T}^{n+1}(r, \hat{\zeta}) \, d\sigma. \tag{59}$$

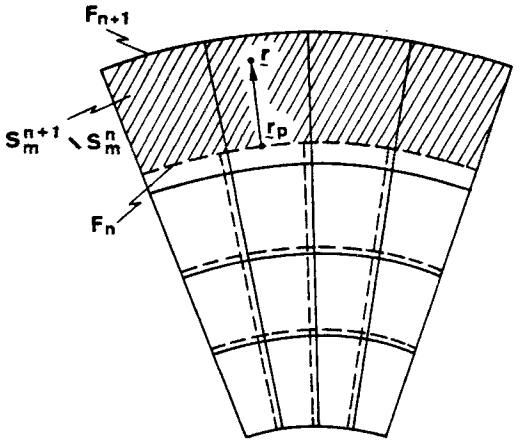

Figure 8. Extrapolation of the temperature field in the region located between two successive fronts.
———, old mesh; ———, new mesh

As $\hat{T}^{n+1}(r, \hat{\zeta})$ is defined on S_m^n, the righthand side of the latter equation must be evaluated by extrapolation when

$$r \in S_m^{n+1} - S_m^n. \tag{60}$$

Let r_p be any projection of r on the initial front F_n of the time interval, Figure 8. The approximation is

$$\hat{T}^{n+1}(r, \hat{\zeta}) = \hat{T}^{n+1}(r_p, \hat{\zeta}) + \nabla\hat{T}^{n+1}(r_p, \hat{\zeta}) \cdot (r - r_p), \tag{61}$$

where the temperature gradient $\nabla\hat{T}^{n+1}$ and the front normal $(r - r_p)/\|r - r_p\|$ are both smoothed in a first step by the Galerkin technique to obtain continuous fields defined on F_n.

The front condition (Eq. 21) is taken into account at this stage: classical Cholesky LL^T factorization is performed for solving Eq. 59 in such a way that all temperature nodal values $T_{j\alpha}^{n+1}$ and T_{jw}^{n+1} are expressed as functions of the nodal values on the new front F_{n+1}. The latter are then computed using Eq. 59 and are corrected following Eq. 21. The remainder of the back-substitution follows and provides all the temperature nodal values.

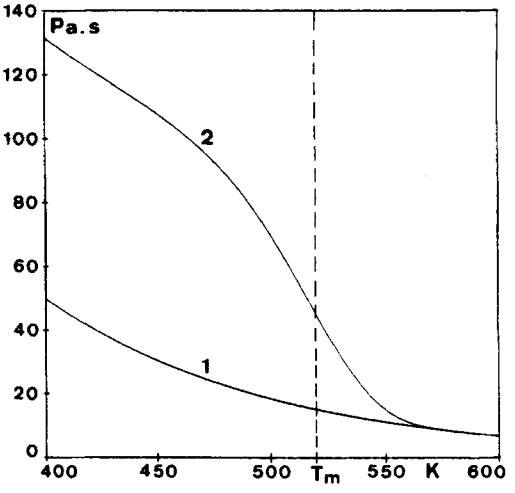

1. Exponential law
2. Modified law ($n' = 20$, $T_m = 520$ K).

Figure 9. Viscosity as a function of temperature.

General scheme of the program

Recalling that a complete filling is simulated in a sequence of time steps, the available results at time t_n are the flow domain S_m^n, the corresponding temporary mesh R_n, the pressure and temperature nodal values p_i^n, $T_{i\alpha}^n$ and T_{iw}^n, the fronts F_n, and the front average velocities $\bar{v}_i^n$.

The solution at time t_{n+1} will be obtained after the following computations:

- Time integration of the temperature field ($\rightarrow \hat{T}_{i\alpha}^{n+1}$ and $\hat{T}_{iw}^{n+1}$)
- Displacement of the fronts ($\rightarrow F_{n+1}$ and S_m^{n+1})
- Remeshing ($\rightarrow R_{n+1}$)
- Extrapolation and correction of the temperature field ($\rightarrow T_{i\alpha}^{n+1}$ and $\rightarrow T_{iw}^{n+1}$)
- Integration of the pressure field ($\rightarrow p_i^{n+1}$)
- Calculation of the front velocities ($\rightarrow \bar{v}_i^{n+1}$)

Results and Discussion

Simulations without front motion

A theoretical example is here considered to illustrate some capabilities of the numerical scheme. A schematic view of the problem is shown in Figure 2. A hot molten polymer is injected through a circular gate and passes between two cold semispherical walls. However, we do not simulate the front motion and all the injected fluid continuously exits from the mold at a given pressure through the circular outlet E. Nevertheless, the studied phenomenon remains transient, since the initial and steady-state temperature fields are different.

For details on the geometry, the mesh, and the data, see Vanderschuren and Dupret (1986) and Supplementary Material, as well as for results concerning isothermal flow or nonisothermal flow with the viscosity law (Eq. 2). We here investigate the influence of a modification of this latter to take into account partial solidification on the walls during filling.

The modified law is defined by:

$$m(T) = m_0 e^{-aT} + m_1 e^{-(T/T_m)^{n'}}, \qquad (62)$$

and was introduced as the first approach of the solidification phenomenon. Observe that when the index n' approaches infinity, the material function $m(T)$ decreases suddenly by a value m_1 when the melting temperature T_m is crossed. Choosing sufficiently high values for n' and m_1, therefore, induces an important increase of the viscosity under T_m. The graph of the material function $m(T)$ is shown in Figure 9 for both laws, Eqs. 2 and 62.

Streamlines, average isotherms, temperature profiles, and velocity profiles are presented in Figures 10 and 11 for the steady-state final solution. As a consequence of the nonsymmetric position of the inlet gate, material points emerging in the vicinity of C in Figure 10 have a higher residence time in the mold than points emerging in the vicinity of B (their path is longer and their velocity smaller). The resulting temperature decrease in the region of C, therefore, induces a viscosity increase which tends to slow down the fluid motion. Pathlines are in that manner strongly deflected. Nevertheless, complete solidification is nowhere observed. Further simulations will deal with investigations on the latter phenomenon.

Let us note that Figure 11 exhibits the good behavior of the Chebyshev collocation method when considering solidification

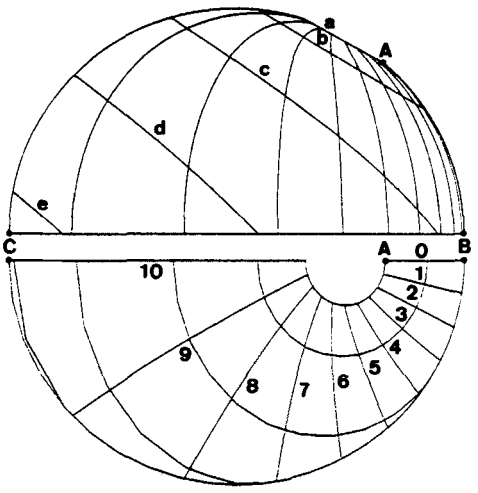

Figure 10. Modified viscosity law.
Streamlines by steps of 0.5 cm³/s; average isotherms from 577 K downwards by steps of −20 K.

on the walls: the velocity gradient is indeed rapidly changing from the solidified layer to the liquid zone, while no oscillations are observed on the figure.

One-dimensional simulations

In view of a clear understanding of the major consequences of the fountain effect, we first consider one-dimensional flows in a 120 mm × 50 mm rectangular mold with a 2-mm gap between two 10-mm steel walls ($k_s = 46$ W · m^{-1} · K^{-1}, $\rho_s c_s = 3.6\ 10^6$ J · m^{-3} · K^{-1}). Injected polymers are either a polyamide or a polycarbonate, and material constants are in Table 1, which was prepared using the viscosity law (Eq. 2). Gate temperature is constant and set to 260°C. External temperature is set to 100°C or 110°C, respectively. The fixed mesh (corresponding to the entire midsurface of the mold) is formed of 30 equal rectangular elements. A set of ten collocation points is used in the gapwise direction. Complete injection was performed in 100 equal time steps, through a rectilinear gate formed by one of the short sides of the mold. The initial front was located 6 mm from this gate.

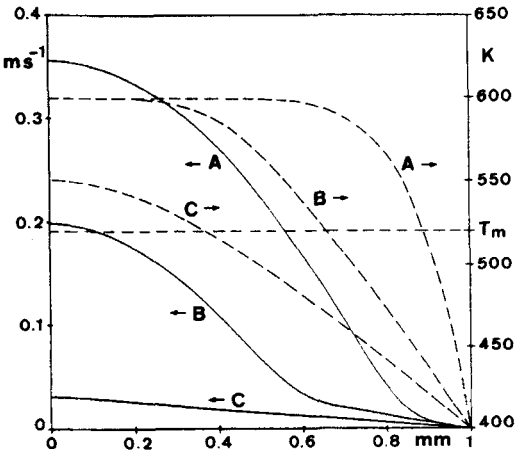

Figure 11. Modified viscosity law.
Temperature and velocity profiles at points A, B and C, as located in Figure 10 (10 collocation points).

A first set of simulations will show off the fountain flow thermal influence by means of a comparison between two ways of building the front thermal model:

1. The problem is properly handled using the conservative method which has been previously described.

2. The fountain effect is ignored and the related correction of the temperature at the front as well; it is well known that this yields a non-conservative model.

In order to simplify discussion, viscous heating is dropped in both cases in the energy equation. Injection is performed at a flow rate of 25 cm^3/s and the chosen polymer is the polyamide.

As shown in Figure 12, each curve corresponds to a definite moment of the process and represents the spatial average value of the temperature within the thickness, as a function of the distance to the gate.

Main observation is the deep influence of the fountain flow on the temperatures. As a matter of fact, the average front temperature is strongly time decreasing when the nonconservative model is used; moreover, at any time, the lowest mean temperature is obtained on the front. These results are the consequences of the heat losses which occur on the front in this case.

On the contrary, the conservative model provides an average front temperature which is only very slightly decreasing with time and the lowest mean temperature is reached upstream of the front for any time. These effects are due to the front feeding with hot fluid issued from internal layers: observe indeed that midsurface and injection temperatures are everywhere close together, even in the case of a decreasing mean temperature upstream of the front, because fluid velocity is at its highest on the midsurface.

The second set of one-dimensional simulations was intended for illustrating realistic flow conditions. Viscous heating was, therefore, kept in the energy equation. A comparison is made here between polyamide and polycarbonate injection; flow rates are 100 cm^3/s, 50 cm^3/s, and 25 cm^3/s in the former case, and 50 cm^3/s and 25 cm^3/s in the latter case, respectively.

Evolution of the average temperatures for polyamide injection is presented in Figure 13, where viscous heating appears to play a major role in the thermal balance. Consider first the largest flow rate, Figure 13a: average temperatures are everywhere

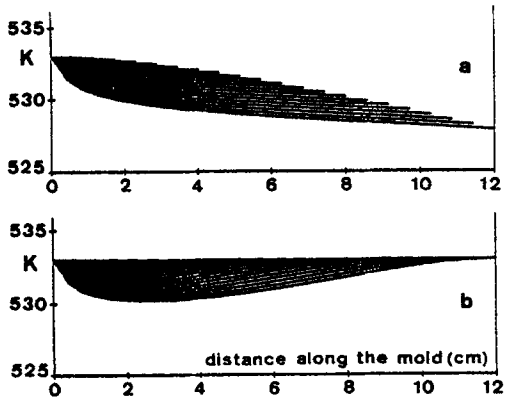

a. Simulation without fountain effect.
b. Simulation with fountain effect.

Figure 12. One-dimensional problem: evolution of the gap average tempeature during filling (no viscous heating).

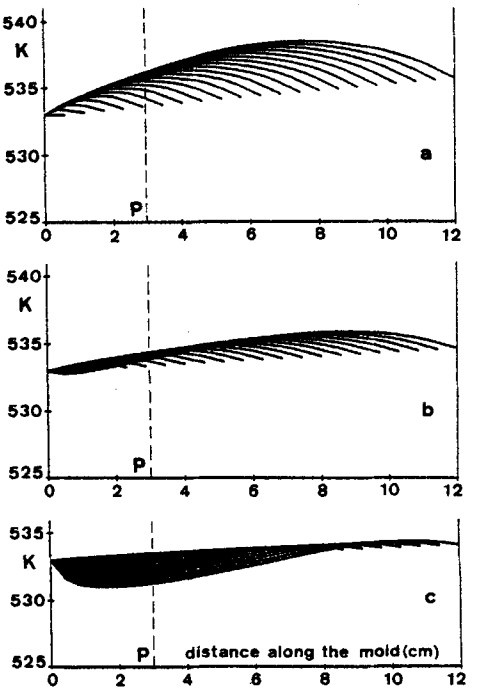

a. Flow rate of 100 cm^3/s (filling in 0.114 s).
b. Flow rate of 50 cm^3/s (filling in 0.228 s).
c. Flow rate of 25 cm^3/s (filling in 0.456 s).

Figure 13. One-dimensional problem: gap average temperature for the injection of a polyamide.

and at any time higher than the injection temperature; furthermore, the highest mean temperature is always obtained upstream of the front. These results are consequences of both viscous heating and fountain effect. Let indeed P be a fixed point on the midsurface and $P'P''$ be the corresponding transverse in the gap. The average temperature of the fluid passing through $P'P''$ is measured on a vertical in Figure 13. Due to the front feeding by fluid issued from internal layers, where viscous heating is low, the starting average temperature on $P'P''$ is close to the injection temperature. Next, slower fluid layers near to the walls arrive at $P'P''$. These layers are warmed by viscous heating, which perfectly agrees with the subsequent increase of average temperature on $P'P''$.

On the other hand, thermal evolution at the lowest flow rate, Figure 13c, is close to the situation without viscous heating, Figure 12. As a matter of fact, shear rate is then reduced, and heat production is, therefore, negligible with respect to heat diffusion in the energy equation.

Evolution at the intermediate flow rate is more complex, Figure 13b. Turning back our attention to the fixed gap transverse $P'P''$, we there observe first an increase and afterwards a decrease of mean temperature. Hence, viscous heating influence appears prior to the cooling effect arising from the walls; while the latter effect is indeed delayed by the time required for diffusion from the walls to more internal (and faster) layers, viscous heating effect is instantaneous.

Evolution of the average temperatures during filling for polycarbonate injection is presented in Figure 14. We also analyze an additional simulation (performed at a flow rate of 50 cm^3/s) where viscous heating was dropped for comparison purposes. As a conclusion, the preceding effects are still observed, but are

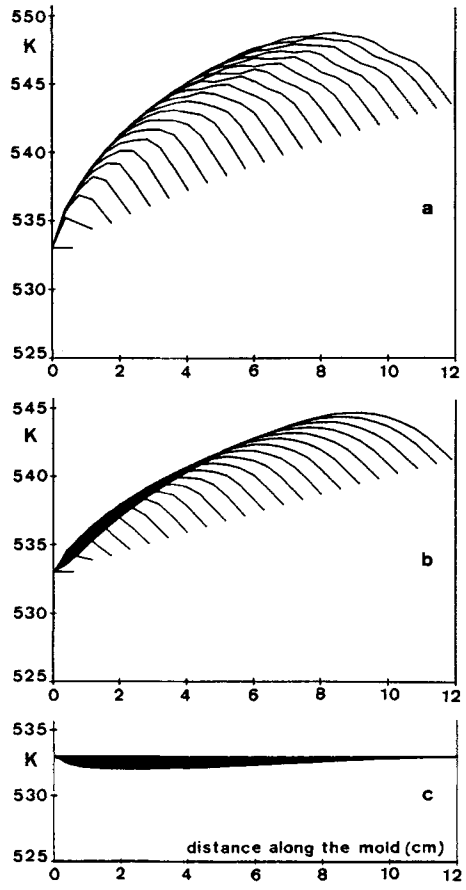

a. Flow rate of 50 cm^3/s (filling in 0.228 s).
b. Flow rate of 25 cm^3/s (filling in 0.456 s).
c. Flow rate of 50 cm^3/s; simulation without viscous heating.

Figure 14. One-dimensional problem: gap average temperature for the injection of a polycarbonate.

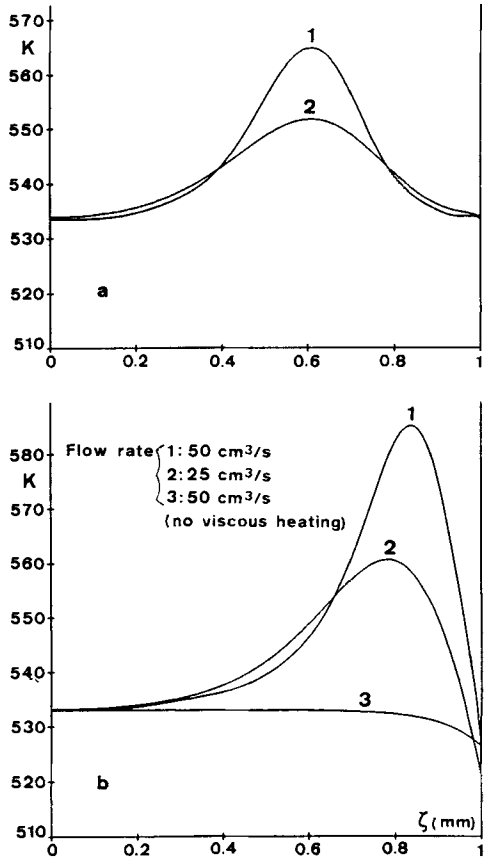

Figure 15. One-dimensional problem: injection of a polycarbonate.
Final temperature profiles on the front (a) and at middistance from the front and the gate (b).

more emphasized, since viscous heating is more important for polycarbonate than for polyamide.

Figure 15 exhibits temperature profiles at the end of the filling, in the case of polycarbonate injection. Figure 15b corresponds to profiles on a transverse equidistant from the front and the gate. A temperature overshoot (due to viscous heating) is observed in the vicinity of the walls. Note here the interest of using a Chebyshev grid, since collocation points are in this manner piled up where the temperature gradient is high.

The front temperature profiles are shown in Figure 15a. These results indicate that viscous heating does not penetrate to the midsurface, but reaches deep fluid layers which move faster than the front (and therefore continuously feed it). The rise of front average temperature observed in Figures 14a and 14b is a consequence of this effect, which also induces nonconstant front temperature profiles, Figure 15a.

Gate pressure is represented as a function of time in Figure 16, in the case of polycarbonate injection. At the lowest flow rate, the curve is almost linear, which means that viscosity dependence on temperature is then negligible, Table 1. The curve is nonlinear at the largest flow rate. Moreover, when the flow rate grows from 25 to 50 cm^3/s, the final gate pressure increases only by about 30%. The latter increase would be of 100% in Newtonian isothermal flow and of 59.1% in isothermal flow with a power index of 0.67 (recall the viscosity dependence on shear rate and temperature in formulas 1 and 2). We conclude that, for polycarbonate injection, a low-pressure increase is required for doubling the flow rate, because viscosity is reduced by both shear thinning and viscous heating. Results cor-

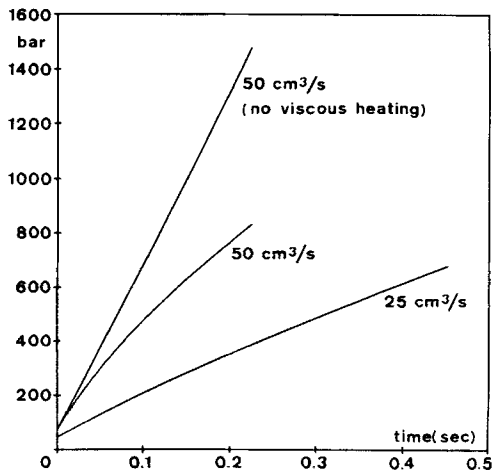

Figure 16. One-dimensional problem: injection of a polycarbonate. Evolution of the gate pressure.

Table 1. Polyamide and Polycarbonate Material Properties

Symbol	Polyamide	Polycarbonate
n	0.75	0.67
a (K^{-1})	0.861×10^{-2}	0.226×10^{-1}
m_0 ($Pa \cdot s^n$)	6.23×10^4	1.44×10^9
k ($W \cdot m^{-1} \cdot K^{-1}$)	0.26	0.215
ρc ($J \cdot m^{-3} \cdot K^{-1}$)	3.04×10^6	2.64×10^6

responding to Figures 15 and 16 for polyamide injection may be found in Supplementary Material.

We can predict a strong influence of all the previously described effects on the solidification phenomenon. On the one hand, a high viscous heating will certainly reduce the solidified layer, especially because heating is important near the walls. On the other hand, a low viscous heating will induce low average temperatures between the gate and the front, where the solidified layer will, therefore, be important (recall that midsurface temperature is close to the gate temperature, whence temperature near the walls must be lowered).

Two-dimensional simulation

By solving a two-dimensional problem, the complete algorithm can be checked under normal conditions. Injection of polyamide is performed in a rectangular mold (dimensioned as in the one-dimensional simulations) through a semicircular gate at a flow rate of 100 cm^3/s. The complete simulation has required about 90 minutes CPU time on a Data General MV/10000 computer. The fixed mesh, the final temporary mesh (corresponding to ⅔ of the filling), and the progression of the flow front are shown in Figure 17. Note that, due to the symmetry of the mold, only one half of the geometry has been considered. The problem is two-dimensional owing to the shape of the gate, but the motion clearly becomes one-dimensional at the end of the filling.

Evolution of the gap average temperature on the plane of symmetry (intersecting the midsurface along *AB* on Figure 17) is presented in Figure 18. The latter is globally very close to the one-dimensional result of Figure 13a. The only difference lies in a steeper increase of mean temperature in the vicinity of the gate, where viscous heating is increased by higher velocities.

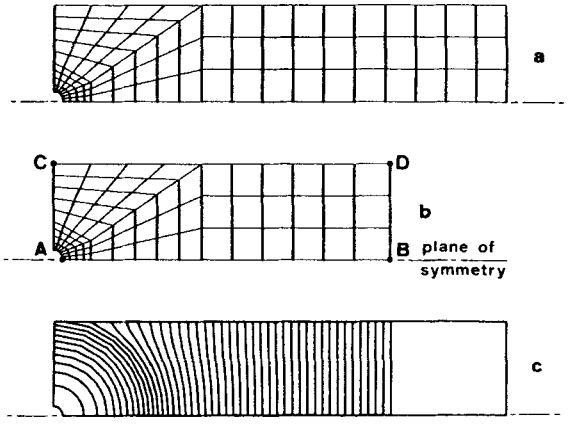

a. Fixed mesh.
b. Temporary mesh at the end of the simulation.
c. Progression of the flow front.

Figure 17. Two-dimensional injection of a polyamide.

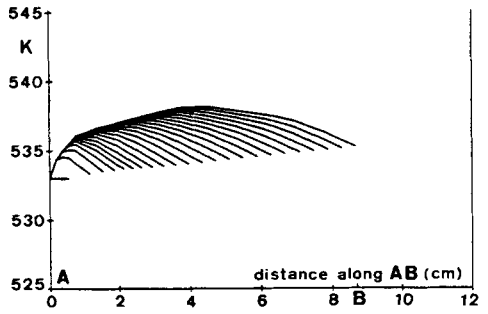

Figure 18. Two-dimensional injection of a polyamide.
Evolution of the gap average temperature on the plane of symmetry.

Gate pressure history is represented in Figure 19. In the beginning of the filling, the flow is purely radial, whence pressure rapidly increases until the corners C and C' are attained by the front. After reorganization of the streamlines, pressure increase is slowed down and remains linear afterwards.

Final average isotherms are represented in Figure 20. The maximum is obtained at the center of the mold, while low values are observed near the front, the gate and the corners C and C'. These effects are consequences of fountain flow and viscous heating (as previously explained), and also of the fact that C and C' are stagnation points, for which fluid slowing down and cooling are important in their vicinity. Observe also that the shortest and fastest path from the gate to the front is the straight segment AB, whence viscous heating is more important in the centrum of the mold.

Conclusions

A hybrid numerical method for predicting three-dimensional thermal effects occurring during the filling of a thin cavity has been developed. The choice of a high-order polynomial representation of the temperature field in the gapwise direction, combined with a finite element discretization in the midsurface direction, appears to be relevant in view of the obtained temperature profiles. The deep influence of fountain flow on the obtained temperature field, as calculated at the end of the filling, has been shown. Further investigations will deal with simulation of partial or complete solidification during the latter stage of the process.

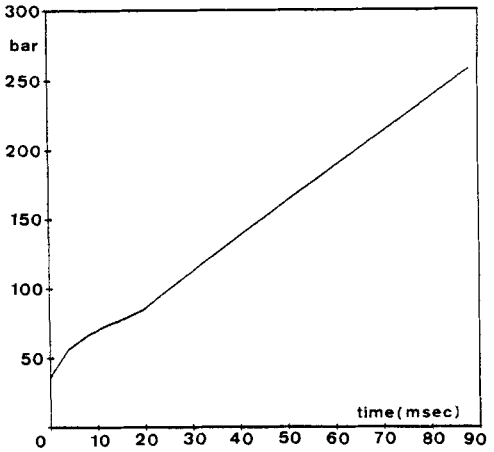

Figure 19. Gate pressure history.

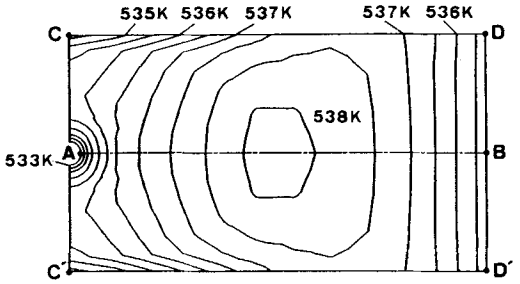

Figure 20. Average isotherms at the end of the simulation.

Acknowledgment

This work was supported by the European Communities, in the frame of the BRITE Project RI1B-0087-F(CD). The authors would like to acknowledge the useful scientific advice of Prof. M. J. Crochet and the French Society La Télémécanique for providing the data used in the simulations.

Notation

A = matrix defined in Eq. 31
a = material constant defined in Eq. 2
a', a'', a''' = defined in Eq. 48
B = matrix defined in Eq. 45
b = defined in Eq. 48
c = polymer specific heat
c_s = wall specific heat
$E(\tilde{z})$ = amplification factor
e = wall thickness
F_n = front at time step t_n
$f(\tilde{y})$ = defined in Eq. 42
$G([p], [T])$ = stiffness matrix defined in Eq. 41
$(\mathbf{g}_\xi, \mathbf{g}_\eta, \mathbf{g}_\zeta)$ = unit base vectors
h = half of the cavity thickness
h_i = nodal values of h
K = matrix defined in Eq. 40
k = polymer thermal conductivity
k_s = wall thermal conductivity
k_1, k_2, k_3, k_4 = defined in Eq. 44
L = characteristic dimension of the midsurface
M = mass matrix defined in Eq. 40
m = number of collocation points
$m(T)$ = material function defined in Eq. 2
m_o = material constant defined in Eq. 2
m_1 = material constant defined in Eq. 62
n = power-law index
$\boldsymbol{n}$ = midsurface constrained outer normal on ∂S_m^*
n' = material constant defined in Eq. 62
p = pressure
p_i = pressure nodal values
$[p]$ = vector of pressure nodal unknowns (p_i)
p_i^n = pressure nodal values at time t_n
$Q_\alpha(\hat{\xi})$ = Lagrange interpolation polynomials
q_e = outgoing external heat flux
q_w = outgoing wall heat flux
$q([T],[p])$ = defined in Eq. 40
R_n = mesh at time step t_n
$\boldsymbol{r}$ = position vector on the midsurface
$\boldsymbol{r}_p$ = projection of $\boldsymbol{r}$ on the previous front
S = defined in Eq. 13
S_m = midsurface
S_m^n = flow domain at time step t_n
S_m^* = filled part of the midsurface
T = temperature
T_e = external temperature
T_m = melting temperature
$T_{2m}(\hat{\xi})$ = $2m$-degree Chebyshev polynomial
T_w = polymer temperature on the wall
$T_i(\hat{\zeta}, t)$ = polynomial temperature profile in the gap at time t
$T_{i\alpha}(t)$ = temperature at node i, time t and collocation point α
$T_{iw}(t)$ = wall temperature at node i and time t
$[T]$ = vector of all temperature unknowns ($T_{i\alpha}$ and T_{iw})
$T^n(\boldsymbol{r}, \hat{\zeta}), \hat{T}^n(\boldsymbol{r}, \hat{\zeta})$ = temperature field at time step t_n
$T_{i\alpha}^n$, T_{iw}^n, $\hat{T}_{i\alpha}^n$, $\hat{T}_{iw}^n$ = temperature nodal values at time step t_n
t = time
D/Dt = material derivative
$\boldsymbol{v}$ = velocity vector
(v_ξ, v_η, v_ζ) = cartesian components of $\boldsymbol{v}$
$\boldsymbol{v}_m$ = midsurface components of $\boldsymbol{v}$
$\overline{\boldsymbol{v}}$ = gap average value of $\boldsymbol{v}$
$\overline{\boldsymbol{v}}_i^n$ = front nodal velocities at time step t_n
(x, y, z) = general Cartesian coordinates
$\tilde{\boldsymbol{y}}$ = vector of all the time-dependent unknowns
$\tilde{\boldsymbol{y}}_n$ = unknowns at time step t_n
$\tilde{z}$ = complex independent variable

Greek letters

$\dot{\gamma}$ = shear rate
Δt = time interval ($t_{n+1} - t_n$)
δ = order of magnitude of the mold thickness
ϵ = dimensionless number, defined in Eq. 18
ζ = Cartesian coordinate in the gap direction
$\hat{\zeta}$ = normalized coordinate in the gap direction
$\hat{\zeta}_\alpha$ = collocation point of index α
θ_{ij} = defined in Eq. 44
λ_i = eigenvalues of B as defined in Eq. 45
μ = shear viscosity
(ξ, η) = first and second Cartesian coordinates in the midsurface direction
$(\hat{\xi}, \hat{\eta})$ = local coordinates on the parent element
ρ = melt density
ρ_s = wall density
ϕ_i = linear or bilinear shape functions
ψ_i = quadratic or biquadratic shape functions
ω = defined in Eq. 53
∇ = gradient operator
∇_m = midsurface constrained gradient operator

Literature Cited

Behrens, R. A., M. J. Crochet, C. D. Denson, and A. B. Metzner, "Transient Free-Surface Flows: Motion of a Fluid Advancing in a Tube," *AIChE J.*, **33**(7), 1178 (1987).

Castro, J. M., and C. W. Macosko, "Studies of Mold Filling and Curing in the Reaction Injection Molding Process," *AIChE J.*, **28**(2), 250 (1982).

Couniot, A., and M. J. Crochet, "Finite Elements for the Numerical Simulation of Injection Molding," *Proc. Int. Conf. on Num. Math. in Ind. Forming Proc.*, 165, Gothenburg, Sweden (1986).

Coyle, D. J., J. W. Blake, and C. W. Macosko, "The Kinematics of Fountain Flow in Mold Filling," *AIChE J.*, **33**(7), 1168 (1987).

Dietz, W., and J. L. White, "Ein Einfaches Modell zur Berechnung des Druckverlustes Während des Werkzeugfüllvorvanges und der Eingefrorenen Orientierung beim Sprietzgiessen Amorpher Kunststoffe," *Rheol. Acta*, **17**, 676 (1978).

Dupret, F., and L. Vanderschuren, "Asymptotical Behaviour of the Equations Governing the Filling Stage in the Injection Molding Process," submitted (1988).

Gottlieb, D., and S. A. Orszag, "Numerical Analysis of Spectral Methods: Theory and Applications," *CBMS-NSF Conf. Ser. Appl. Math.*, 26, SIAM, Philadelphia (1977).

Hadamard, J., "La Théorie des Équations aux Dérivées Partielles," Editions Scientifiques, Pékin (1964).

Hieber, C. A., "Injection and Compression Molding Fundamentals," A. I. Isayev, Ed., Marcel Dekker, New York (1987).

Hieber, C. A., and S. F. Shen, "A Finite Element/Finite-Difference Simulation of the Injection-Molding Filling Process," *J. Non-Newt. Fluid Mech.*, **7**(1), (1980).

Jain, M. K., "Numerical Solution of Differential Equations," Wiley Eastern Line, New Delhi (1979).

Janeschitz-Kriegl, H., "Injection Moulding of Plastics: Some Ideas

about the Relationship between Mould Filling and Birefringence," *Rheol. Acta,* **16,** 327 (1977).
———, "Injection Moulding of Plastics: II. Analytical Solution of Heat Transfer Problem," *Rheol. Acta,* **18,** 693 (1979).
Lapidus, L., and J. M. Seinfeld, *Numerical Solution of Ordinary Differential Equations,* Academic Press, New York (1971).
Lord, H. A., and G. Williams, "Mold-Filling Studies for the Injection Molding of Thermoplastic Materials: Part II. The Transient Flow of Plastic Materials in the Cavities of Injection-Molding Dies," *Polym. Eng. Sci.,* 15(8), 569 (1975).
Manas-Zloczower, I., J. W. Blake, and C. W. Macosko, "Space-Time Distribution in Filling a Mold," *Polym. Eng. Sci.,* **27**(16), 1229 (1987).
Richardson, S. M., "Injection Moulding of Thermoplastics: Freezing During Mould Filling," *Rheol. Acta,* **22,** 223 (1983).
Schlichting, H., "Boundary-Layer Theory," McGraw Hill, New York (1968).
Shen, S. F., "Polymer-Flow Modelling and Simulation of the Injection-Molding Process," *Proc. Int. Conf. on Num. Math. in Ind. Forming Proc.,* Gothenburg, Sweden, 51 (1986).
Tadmor, Z., and C. G. Gogos, *Principles of Polymer Processing,* Wiley (1979).
Tayler, A. B., and M. O. Nicholas, "Unsteady Slow Flows Over a Cooled Flat Plate," *IMA J. Appl. Math.,* **28,** 75 (1982).
Vanderschuren, L., and F. Dupret, "Three-Dimensional Calculation of the Temperature Field during Injection Molding," *Proc. Int. Conf. on Num. Math. in Ind. Forming Proc.,* Gothenburg, Sweden, 199 (1986).
———, "Simulation Numérique de l'Influence Thermique de l'Écoulement Fontaine dans le Procédé de Moulage par Injection," Actes du Premier Congrès National Belge de Mécanique Théorique et Appliquée, M. Deville and P. Sas, eds., Brussels, Belgium, 180 (1987).
Van Wijngaarden, H., J. F. Dijksman, and P. Wesseling, "Nonisothermal Flow of a Molten Polymer in a Narrow Rectangular Cavity," *J. Non-Newt. Fluid Mech.,* **11,** 175 (1982).
Williams, G., and H. A. Lord, "Mold-Filling Studies for the Injection Molding of Thermoplastic Materials: Part I: The Flow of Plastic Materials in Hot- and Cold-Walled Circular Channels," *Polym. Eng. Sci.,* **15**(8), 553 (1975).

Manuscript received Feb. 9, 1988, and revision received July 7, 1988.

See NPAS document no. 04628 for 6 pages of supplementary material. Order from NAPS c/o Microfiche Publications, P.O. Box 3513, Grand Central Station, New York, NY 10163. Remit in advance in U.S. funds only $7.75 for photocopies or $4.00 for microfiche. Outside the U.S. and Canada, add postage of $4.50 for the first 20 pages and $1.00 for each of 10 pages of material thereafter, $1.50 for microfiche postage.